Electronic Supplementary Information for

Tailoring preferable orientation relationship and shape of α-$FeSi_2$ nanocrystals on Si(001): impact of gold and Si/Fe flux ratio, origin of α/Si boundaries

Ivan A. Tarasov,*[a] Tatiana E. Smolyarova[a,b], Ivan V. Nemtsev[a,c], Ivan A. Yakovlev[a], Mikhail N. Volochaev[a], Leonid A. Solovyov[d], Sergey N. Varnakov[a], Sergey G. Ovchinnikov[a,c]

[a]Kirensky Institute of Physics, Federal Research Center KSC SB RAS, Krasnoyarsk, 660036 Russia [b]Siberian Federal University, 660041, Krasnoyarsk, Russia

[c]Federal Research Center KSC SB RAS, Krasnoyarsk, 660036, Russia

[d]Institute of Chemistry and Chemical Technology, Federal Research Center KSC SB RAS, 660036 Krasnoyarsk, Russia

*Corresponding author email: tia@iph.krasn.ru

METHODS

Preparation of α-$FeSi_2$ nanocrystals

It is known the surface conditions along with the atom flux and substrate temperature cause the appearance of the particular form and orientation of a certain iron silicide nucleated on or in the silicon substrate. Thus, we could create only one type of the silicide crystalline shape and its OR with a silicon substrate having an ideal singular silicon surface and uniform temperature, along with homogeneous flux distribution of incoming atoms over the substrate. Then, simultaneous nucleation of the different types of iron silicide nanocrystals becomes more possible with entering varied defects into the silicon surface. The temperature may play a key role in the formation sequence of the higher iron silicides (α, β, γ, s-$FeSi_2$). According to our preliminary calculations (not presented here), the misfit for γ-$FeSi_2$/Si hetero-system increases with the temperature, whereas for α-$FeSi_2$/Si one it decreases. The interplanar spacing misfit of α-$FeSi_2\{110\}$//Si{022} is expected to be zero close to 850 °C, while at the same temperature for γ-$FeSi_2\{022\}$//Si{022} pair it becomes significantly larger than at the room temperature, of about -1 %. Thus, at a temperature around 850 °C, the growth of α-$FeSi_2$ phase should take place. Moreover, from a thermodynamic view, a γ-$FeSi_2$ compound is a non-existent phase in bulk conditions. In turn, the formation of γ- and s-$FeSi_2$ phases may occur under lower temperatures in nanoislands. Earlier, we showed[1] time-dependent sequence of the phase formation γ-$FeSi_2$ → β-$FeSi_2$ at 630 °C[2] and the growth of α-$FeSi_2$ on 1°- miscut Si(001) surface with multiple ORs and nanocrystal shapes at 840 °C. Such sensitivity to the temperature allowed us to grow α-$FeSi_2$ nanocrystals and focus on finding how to handle their ORs and shapes on the Si(001) substrate, which is technologically important for the industry. The changes in the ratio of Si/Fe flux deposited onto gold-free or gold-activated Si(001) surface was implemented to alter the α-$FeSi_2$ growth conditions.

The samples AFS-1-4 and AFSS-1-4 were obtained at the temperature of 840 °C under the only Fe flux with the iron deposition rate of 0.17 nm/min ($\frac{\upsilon_{Si}}{\upsilon_{Fe}} = 0$), and the ($\frac{\upsilon_{Si}}{\upsilon_{Fe}} = 3.4$), respectively. The rate of Si deposition was 0.58 nm/min. Prior to the iron deposition the different amount of gold was deposited at a rate of 0.23 nm/min: ASF-1, AFSS-1 – 3 nm, ASF-2, AFSS-2 – 7 nm, ASF-3, AFSS-3 – 10 nm and ASF-4, AFSS-4 – 15 nm. Additional information on the AFFS and ASF series, including resultant Au/Fe atomic per cent ratio, can be found in Table S1, S2.

RESULTS AND DISCUSSION

Morphology and crystal structure characterisation

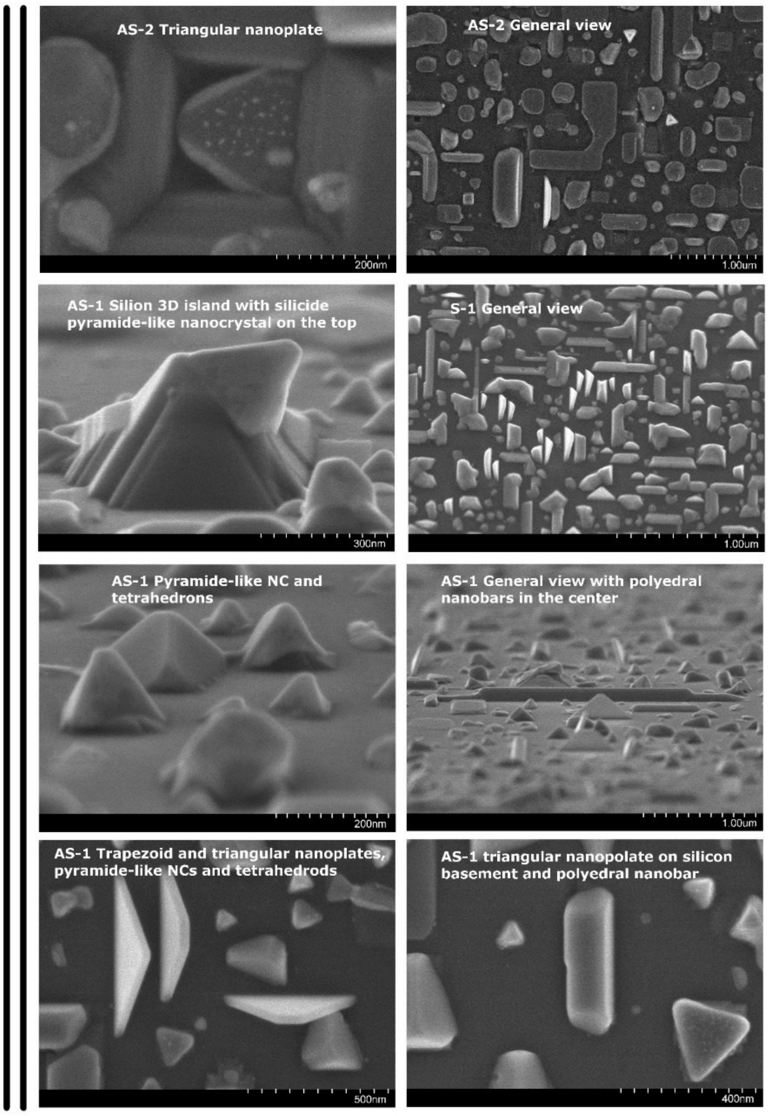

Fig. S1 SEM images of α-$FeSi_2$ nanocrystals grown on gold-activated and gold-free surfaces Si(001). Correspondence to the sample obtained is given on the images.

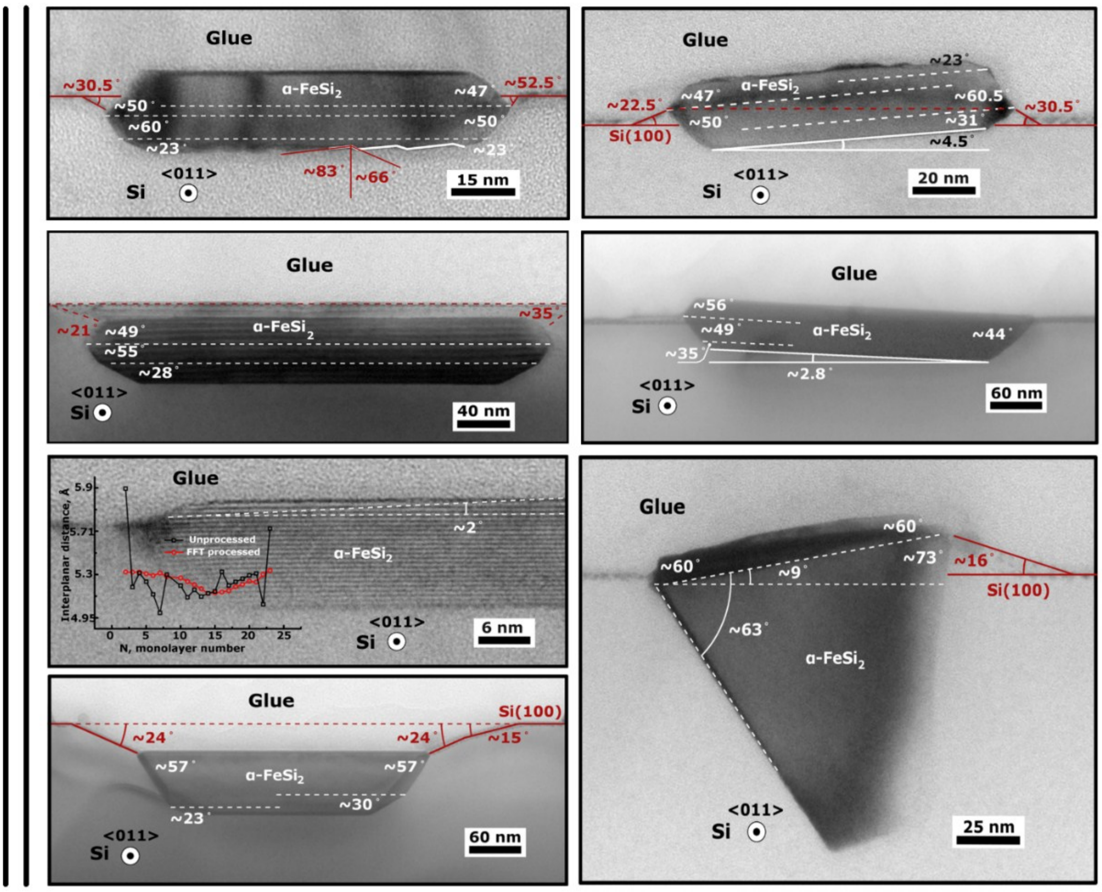

Fig. S2 TEM images of α-FeSi$_2$(001)//Si(001) nanocrystals obtained on AS1 and AS2 samples.

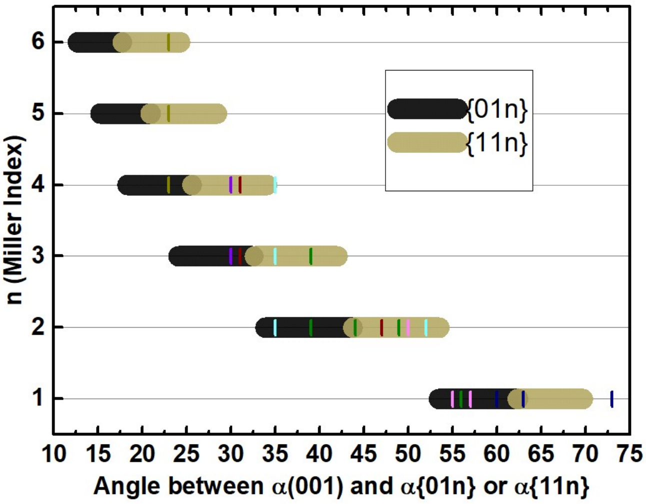

Fig. S3 Possible correspondence of observable angles between α(001) plane and the side facets to α-FeSi$_2$ planes, α{01n} or α{11n} creating side α/Si interface; Black and yellow zones on the figure depicts a range of angles observable, which may correspond to α{01n} and α{11n} side facets. Lines coloured point the angles observed on TEM images of α-FeSi$_2$ nanocrystals.

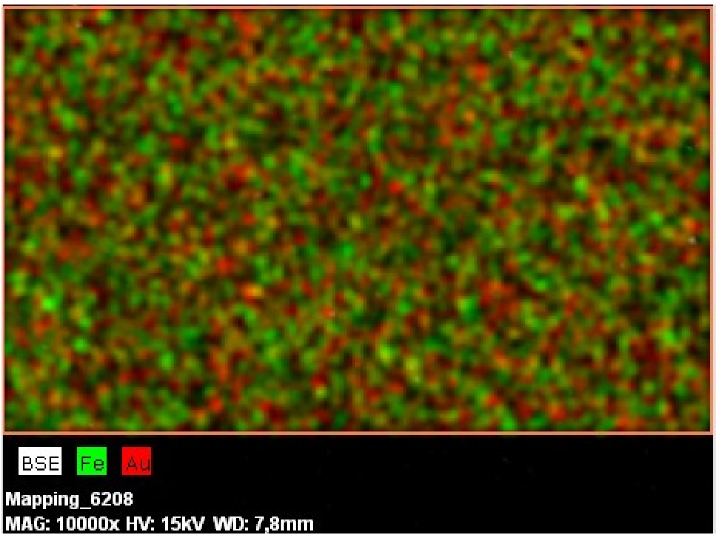

Fig. S4 The result of chemical surface analysis of the AS1 sample carried out with the help of Hitachi TM 3000.

Role of gold layer in formation of nanocrystals

Apart from the nanocrystals denoted in the article another type exists, which have greater sizes (Fig. S1, S5) and possess a form of truncated pyramids for the sample AS1. The height of them reaches 550 nm, the length of edges ranging from 700 nm to 1 μm. Formation of such nanocrystals may occur due to a combination of two factors corresponded to the AS1 sample, which are silicon rich atomic flux and the presence of gold.

Thus, these 3D islands are supposed to be made from silicon with the gold droplets on the top (Fig. S5). Their side facets are inclined relatively to Si(001) surface with an angle close to 54°, which corresponds to Si{111} planes. The simultaneous growth of the α-$FeSi_2$ nanocrystals on their side facets is possible as well, as can be easily seen in Fig. S1, S5. In turn, the silicon 3D island discussed is not observable on the sample obtained under conditions of the gold-free silicon surface with silicon-rich Si/Fe flux ratio of 3.4 (sample S1), not in the case of the gold-activated surface with iron-rich Si/Fe flux ratio equal to 0.57 (sample AS2).

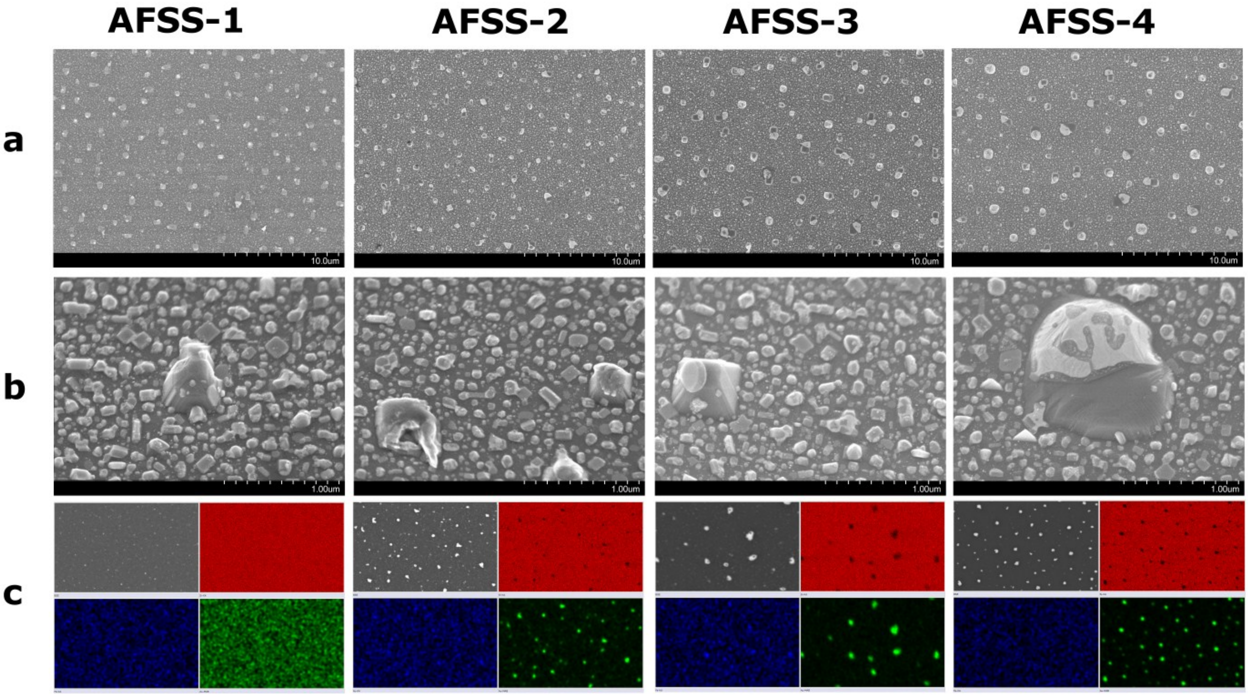

Fig. S5 Surface SEM images of AFSS-1-4 samples (a) on large scale (b) magnified the view of the silicon truncated pyramids (c) Chemical composition surface distribution map, grey inset corresponds to the original SEM image, red – silicon, blue – iron, green - gold.

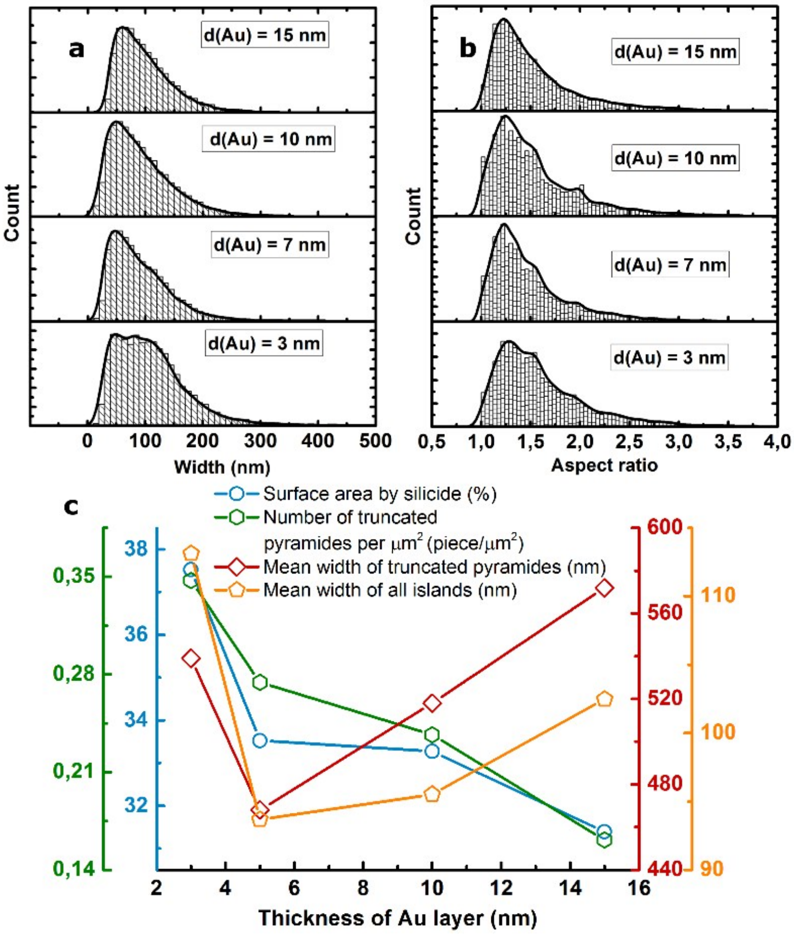

Fig. S6 Lateral size distribution of the nanocrystals (a); aspect ratio distribution of the nanocrystals (b); statistical data illustrating an influence of predeposited gold layer on the growth of α-$FeSi_2$ nanocrystals at Si/Fe atomic flux ratio of 3.4 (c).

Table S1 Normalized chemical composition of the iron and gold deposited on the silicon substrate for AFSS-1-4 samples.

	Atomic per cent, %		Mass per cent, %	
	Au	Fe	Au	Fe
AFSS-1	33.80	66.20	35.70	64.30
AFSS-2	46.90	53.10	75.70	24.30
AFSS-3	44.05	55.95	73.52	26.48
AFSS-4	67.53	32.47	88	12

Additional series of the samples (AFSS-1, 2, 3, 4) with varying the gold layer thickness (3, 7, 10, 15 nm) was obtained under the same Si/Fe flux ratio and synthesis temperature conditions as in the case of the AS1 sample to indicate the role of the gold layer in the formation of the truncated pyramids. The density of the truncated pyramids decreases from 0.35 pieces/μm^2 to 0.15 piece/μm^2, while their average lateral size increases from 0.46 μm up to 0.6 μm (Fig. S6c). However, at the thickness of the gold layer of 3 nm, the mean width of the truncated pyramids (0.54 μm) and the rest of the nanocrystals (0.1 μm) turns out to be larger than for the higher thickness of gold layer (except for d_{Au} = 15 nm in the case of the mean width of the truncated pyramids). This phenomenon is controversial and requires further investigation. The surface area occupied by silicide nanocrystals demonstrates the tendency for vertical growth of the nanocrystals with the increase of gold deposited so it decreases by 7%. This is due to bigger gold-silicon alloy islands attracting more atoms from the surrounding area.

Aspect ratio distribution at the low thickness of the gold layer (3-10 nm) tends to demonstrate discrete peaks at 1.2, 1.5, 1.8, 2.3, whereas at the highest thickness of gold layer it smears (Fig. S6b), attempting to reach homogeneity with the main peak of aspect ratio situated around 1.2. One can conclude the increase of the amount of gold on the surface promotes isotropic growth of silicide nanocrystals, while in the absence of gold, kinetics is regulated by surface energies of only silicon/silicide interfaces resulting in anisotropic growth. Fig. S6a also shows a uniform size distribution with a maximum at 50 nm, whilst with the least amount of the gold predeposited the distribution may be decomposed in two fractions with a maximum at 45 and 100 nm (Fig. S6a). The mean nanocrystal width is estimated to be 115 nm for d_{Au} = 3 nm and decreases down to 98 nm while increasing gold up to 15 nm yields to a gradual increase up to 103 nm.

Chemical surface analysis performed by energy-dispersive X-ray spectroscopy (EDS) on AS1 and AFSS-series reveals the gold is uniformly distributed on the AS-1 (d_{Au} = 1 nm) and AFSS-1 (d_{Au} = 3 nm) samples (Fig. S4 and Fig. S5, respectively). With the increase of the quantity of gold deposited, gold droplets separated become easily distinguishable on EDS maps (Fig. S6 – AFSS-2, 3, 4 samples). The location of such gold droplets coincides with the location of large truncated pyramids. Thus, one can conclude that gold slightly affects the morphology of the main fraction of nanocrystals, resulting in preferred isotropic growth and mainly promotes the formation of relatively large truncated pyramids under silicon-rich growth conditions ($\frac{\upsilon_{Si}}{\upsilon_{Fe}} = 3.4$).

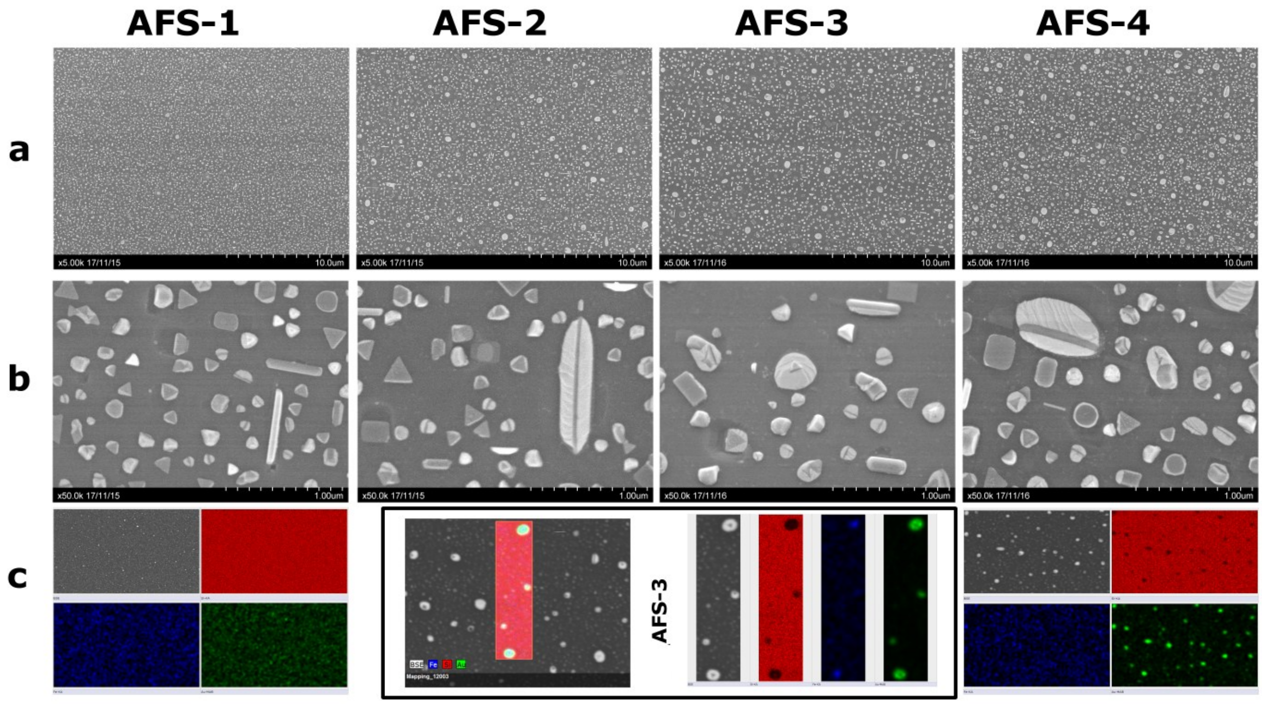

Fig. S7 Surface SEM images of AFS-1-4 samples (a) on large scale (b) magnified view of the sample surface (c) Chemical composition surface distribution map, grey inset corresponds to the original SEM image, red – silicon, blue – iron, green - gold.

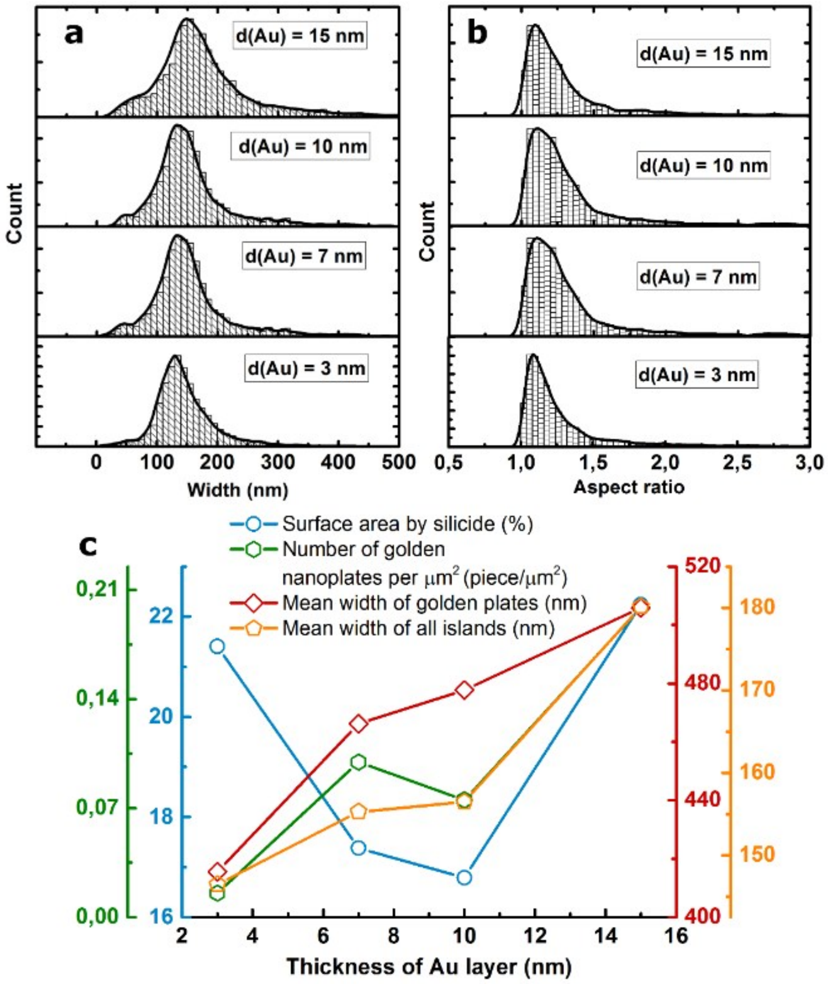

Fig. S8 Lateral size distribution of the nanocrystals (a); Aspect ratio distribution of the nanocrystals (b); statistical data illustrating an influence of predeposited gold layer on the growth of α-$FeSi_2$ nanocrystals at Si/Fe atomic flux ratio of 0 (c).

Table S2. Normalised chemical composition of the iron and gold deposited on the silicon substrate for AFS-1,3,4 samples.

	Atomic per cent, %		Mass per cent, %	
	Au	Fe	Au	Fe
AFS-1	50.64	49.36	78.35	21.65
AFS-3	51.98	48.02	79.24	20.76
AFS-4	60.66	39.34	84.47	15.53

AFS sample series (AFS-1-4) with different thicknesses of gold layers (3, 7, 10, 15 nm) predeposited onto silicon Si(001) surface was prepared to highlight the role of the gold particles in formation of α(001)//Si(001) nanocrystals and to determine their location. As was noted above, the surface density of flat α(001)//Si(001) nanocrystals (*rectangular* and *triangular nanoplates*) is regulated by the Si/Fe flux ratio. Taking into account that an enrichment of the atomic flux with iron increases numbers of the flat α(001)//Si(001) α-$FeSi_2$ nanocrystals growing on Si(001) surface the ASF sample series was synthesised under the Si/Fe = 0 condition. i.e. only iron was deposited.

Consequently, further enrichment of the atomic flux with iron atoms does not drastically change the morphology of the nanocrystals growing. The preferred basic OR remains α(001)//Si(001) and the nanocrystals mainly form as *rectangular* and *triangular nanoplates* (Fig. S7). However, one can notice a formation of Au/α-$FeSi_2$/Au hetero-structures under conditions of the excess of gold (Fig. S7b), where thin α-$FeSi_2$ nanocrystal (~20 nm wide and ~ 1.2 μm long) is laminated between two gold layers. The formation of this self-assembled Au/α-$FeSi_2$/Au heterostructures may be due to higher diffusion of Fe atoms in Si<110> direction. The high aspect ratio of gold lamina reveals that epitaxial OR of the α-$FeSi_2$ island influences strongly the morphology of gold island shape. The ORs, which stimulates anisotropic growth of α-$FeSi_2$ nanocrystals, results in the transformation of initially isotropic gold droplets into gold laminae, whereas the isotropic silicide nanocrystals do not result in prolongation of the gold island (Fig. S7).

Energy-dispersive X-ray mapping (Fig. S7c) and the observation of contrast on the SEM images (Fig. S1, S2) clearly show gold is non-uniformly distributed over the silicon surface for higher thickness values (d_{Au} = 10, 15 nm). Large gold droplets enclose the α-$FeSi_2$ nanocrystals, whereas initially smaller gold droplets are distributed over the α-$FeSi_2$ nanocrystal edges (Figure S7). As in the case of AFSS sample series (Si/Fe = 3.4; d_{Au} = 3, 7, 10, 15 nm), the greater amount of gold deposited the greater number of such nanocrystals per μm^2 (golden nanoplates, Fig. S8c). Moreover, the increase in the amount of gold predeposited alternates the mean lateral size of the nanocrystals so it increases, while the surface area occupied by the nanocrystals decreases (Figure S8c). A higher value of surface area occupied by the nanocrystals at a gold thickness equal to 15 nm may be caused by a general increase of the material deposited on the substrate. One can notice that comparatively to the growth condition with the Si/Fe atomic flux ratio equal to 3.4 the absence of silicon in atomic flux along with the increase in the amount of gold predeposited results in broadening of the lateral size distribution of the nanocrystals (Fig. S8a). Additionally, it increases initially small fraction of nanocrystals with an average size of about 50 nm (Fig. S8a). Broadening is also observable on the distribution of the aspect ratio of nanocrystals (Fig. S8b). In the case of the iron-rich flux, the gold promotes anisotropic growth of nanocrystals increasing their amount with an aspect ratio higher than 1.2 (Fig. S8b, $\frac{\upsilon_{Si}}{\upsilon_{Fe}} = 0$). This is in contrast to silicon-rich conditions (Fig. S6b, $\frac{\upsilon_{Si}}{\upsilon_{Fe}} = 3.4$).

α-$FeSi_2$(001)[010]//Si(001)[010]&[110]

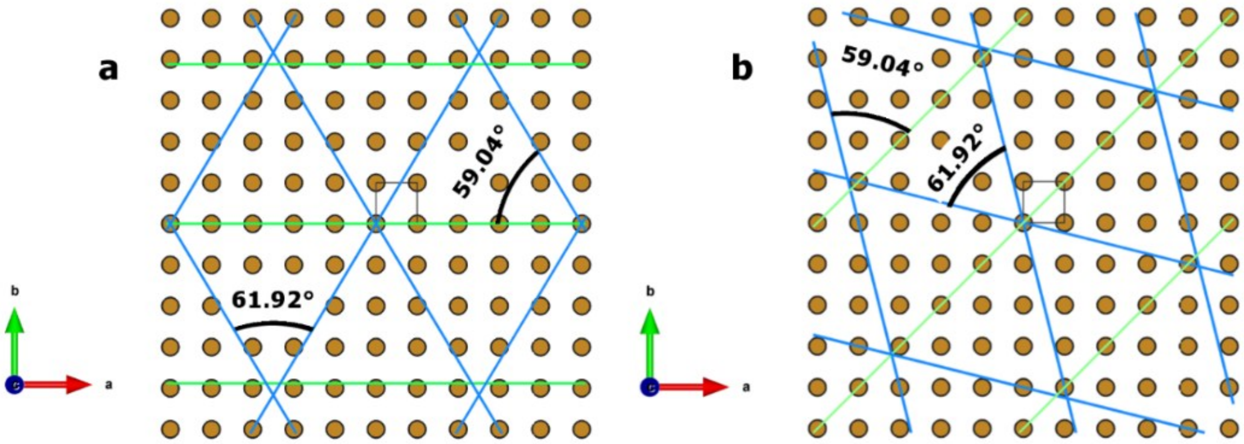

Fig. S9 Schematic illustration of possible spatial alignment of α-$FeSi_2$(001)//Si(001) triangular nanoplates. Green lines correspond to α{01n} or α(11n) or planes and blue lines – α{2 1.2 n} or α{41n} in (a) and (b), respectively. Iron atoms in α(001) plane are depicted with brown colour, c vector points at α<001>.

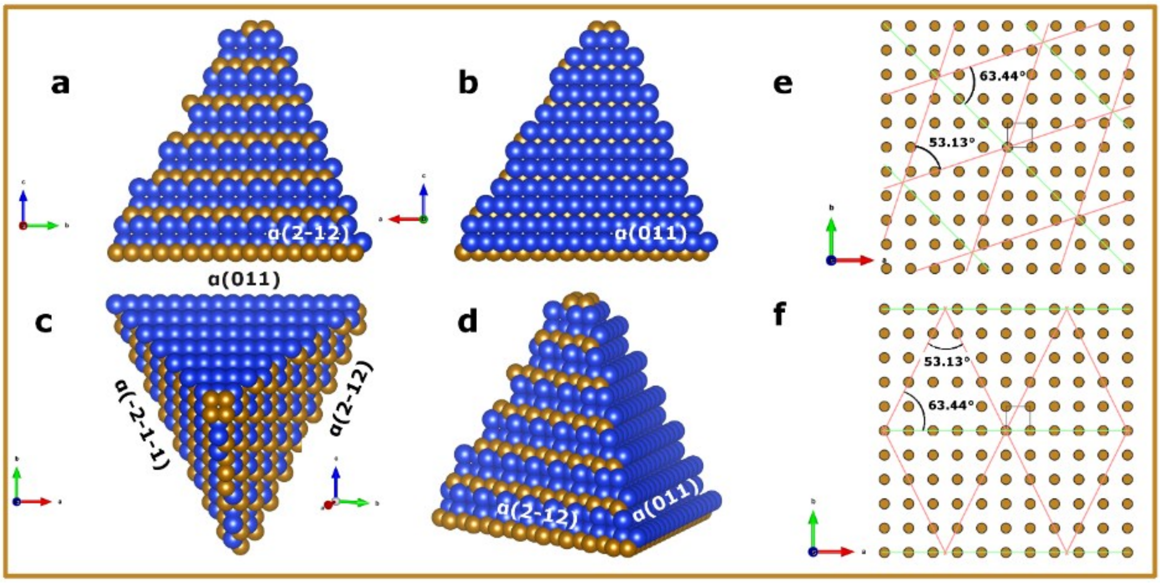

Fig. S10 (a-d) Atomistic illustration of pyramid-like nanocrystal with the basic α(001)//Si(001) OR; (e,f) schematic illustration of possible spatial alignment of α-$FeSi_2$(001)//Si(001) pyramid-like nanocrystals. Green lines correspond to α{11n} or α(01n) or planes and red lines – α{13n} or α{21n} in (e) and (f), respectively. Iron atoms in α(001) plane are depicted with brown color, c vector points at α<001>.

NCS density of interfaces

Fig. S11a, b and S12a, b represent NCS density plotted as function of rotation angles φ and Θ, which correspond to rotation around α[010] or α[100] directions in α-$FeSi_2$(001)[010]||Si(001)[010]&[110] heterostructures. Thus, NCS density at Θ = 0°, φ = 0° depicts its value for α-$FeSi_2$(001)[010]||Si(001)[010]&[110] habit planes. Changes of the Θ angle from 0° to 90° at φ = 0° reveal the NSC density on calculated α||Si interfaces formed by planes from α(001) to α(100), at Θ = 0° and 0° ≤ φ ≥ 90° from α(001) to α(010), at Θ = 90° and 0° ≤ φ ≥ 90° from α(100) to α(010). Hence, a prolonged area with high NCS density situated in range of φ ~ 90° and 0° ≤ Θ ≥ ~30° and φ ~ 90° and 0° ≤ Θ ≥ ~90° in Fig. S11a, b, Fig. S12a, b, respectively corresponds to the high NCS density in interface created by α(010)||Si(010) planes, with small deviations within 1° from α(010) plane, for α(001)[010]//Si(001)[010] basic OR. In the case of α(001)[010]//Si(001)[110] basic OR it refers to α(010)||Si(110) habit planes. NCS maps are given for two types of the calculations of the NCS density with respect to the total amount of atoms in α-$FeSi_2$ planes (Fig. S11a and S12a) or in silicon planes (Fig. S11b and S12b).

As one can see the NCS density maps for the α(001)[010]//Si(001)[010] basic OR (Fig. S11a, b)) are characterised by the presence of a large area with a high NCS density within ranges of φ, Θ angles 0° ≤ φ, Θ ≥ ~20°, and small spots of high NCS density radially distributed from the φ, Θ = 0° point. The large area of high NCS density close to φ, Θ = 0º indicates the favourable conditions for the formation of α(001)||Si(001) zigzag, stepped and flat interfaces. These phenomena are also observable in our experimental TEM images of the nanoplates (Fig. S2). The α(001)//Si(001) embedded nanocrystals have a zigzag interface with silicon along α(001) plane. Angles of deviation from α(001) plane for the zigzag pattern are ~17° (terrace) and ~34°(step).

Let us name radially distributed spots of high NCS density an NCS ray. Thus, the ray corresponded to the deviation from α(001) to α(110), as one can trace, is the most noticeable. Variation of observable angles between α(001) plane and the side facets in the experiment (Fig. S3) coincide with angles formed by α(11n), where n = 1, 2, 3, 4, 5, 6, and α(001) planes, which also indicates correspondence with the NCS map.

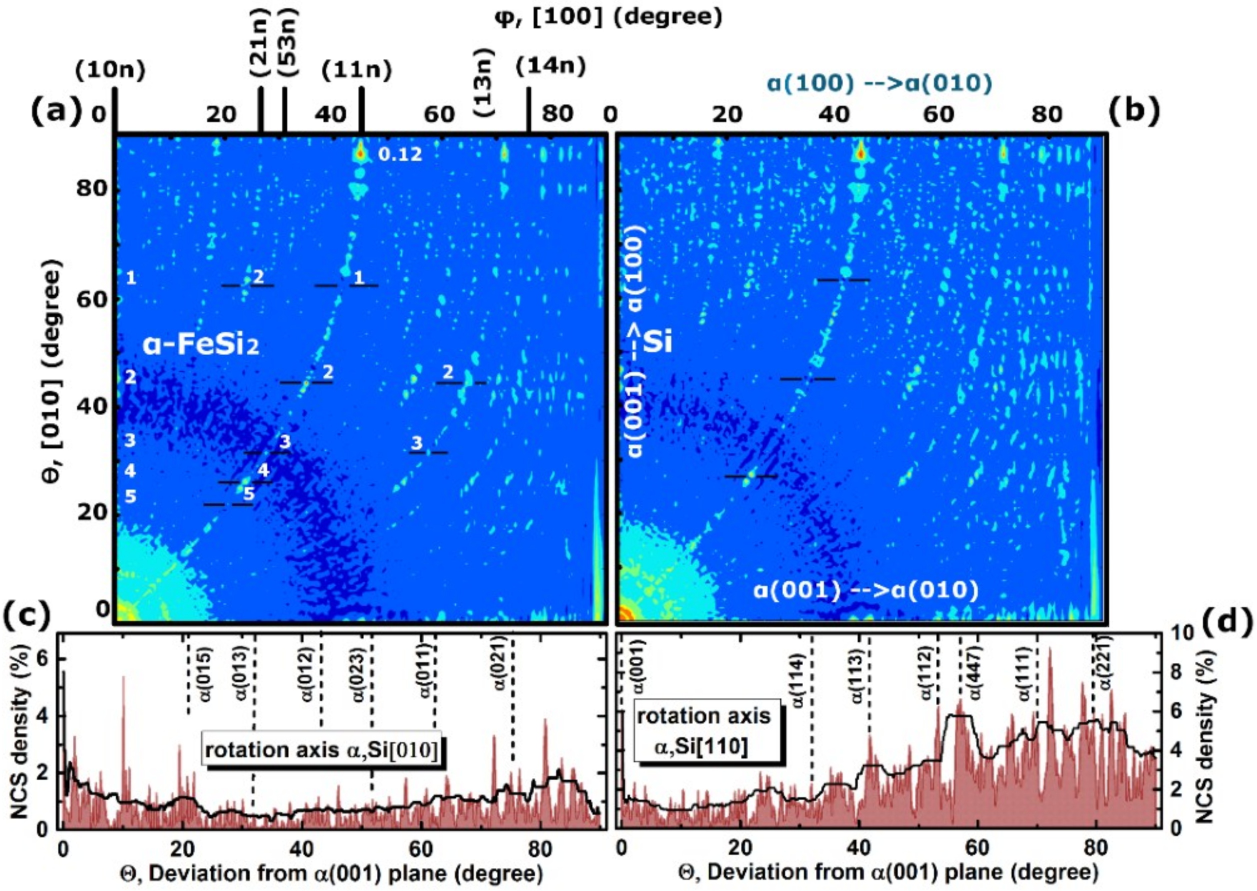

Fig. S11 NCS density maps for α(001)[010]//Si(001)[010] OR. The NCS density is the ratio between a quantity of NCS in a habit plane (120x120 Å, step interval is 0.5°) and quantity of atoms in (a) α-$FeSi_2$ or (b) silicon compound; (c) mean NCS distribution line calculated at rotation around α, Si[010] direction starting from α,Si(001) plane (400x400 Å, step interval is 0.1°), (d) – around α, Si[110] direction; Black lines on (c) and (d) depicts smoothed the distribution line with percentile filter (70 percentile).

One can see that the α(111) plane (φ = 41.5°, ϴ = 62.4°) has a low NCS density. In turn, the TEM examination did not reveal any facet with angle corresponded to α(111) plane, whereas angles matching α(112) range of projection angles occur frequently (Fig. S3). The NCS map at φ = 34.6°, ϴ = 43.7°, α(112), demonstrates one of the highest values. The NCS maps for α(001)[010]//Si(001)[110], in general demonstrating lower NCS densities in comparison with α(001)[010]//Si(001)[010], reveal that α(11n) ray still is an option for formation side facets of nanoplates. A high-density spot is also found at φ = 44.9°, ϴ = 86.4° (Fig. S11). These coordinates

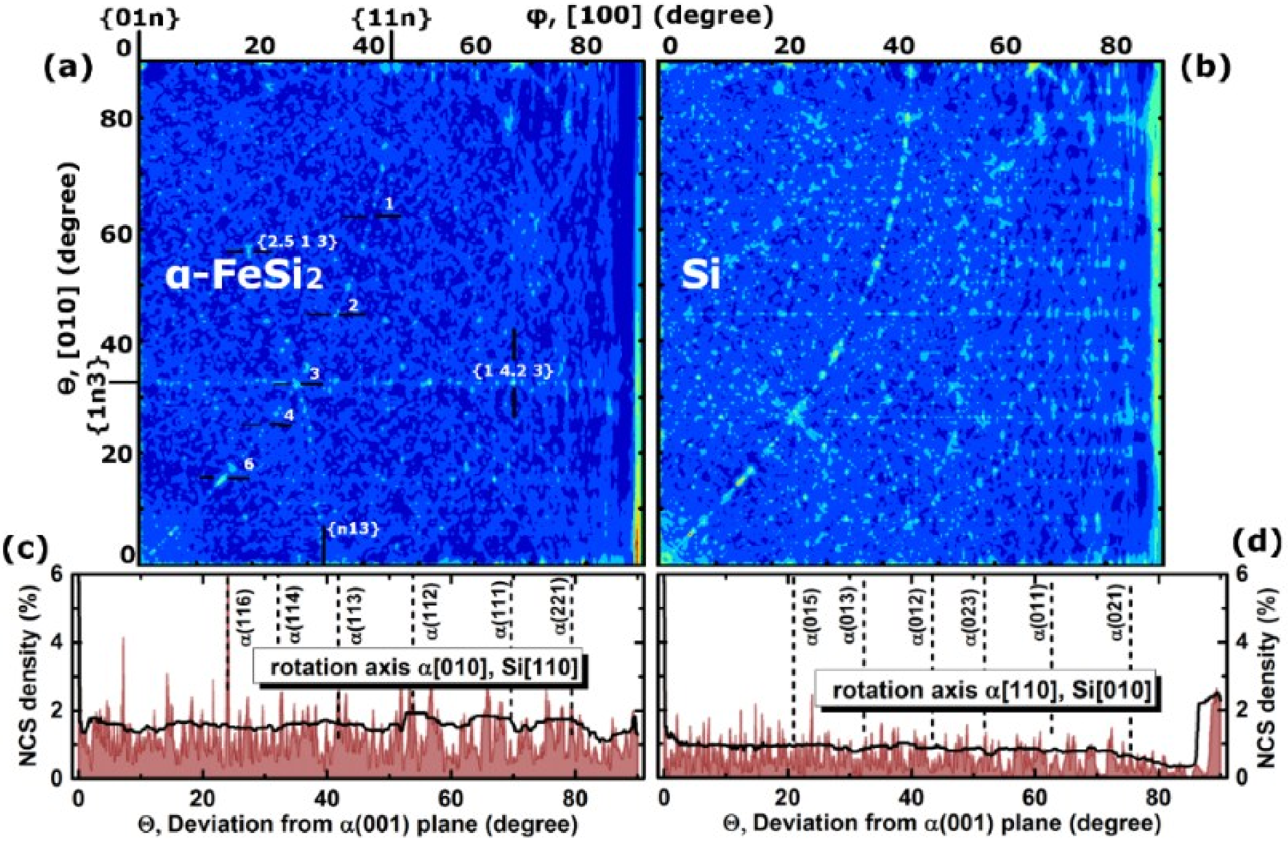

Fig. S12 NCS density maps for α(001)[010]//Si(001)[110] OR. The NCS density is the ratio between a quantity of NCS in a habit plane (120x120 Å, step interval is 0.5°) and quantity of atoms in (a) α-FeSi$_2$ or (b) silicon compound; (c) mean NCS density distribution line calculated at rotation around α[010], Si[110] direction starting from α,Si(001) plane (400x400 Å, step interval is 0.1°), (d) – around α[010],Si[110] direction. Black lines on (c) and (d) depict smoothed the distribution line with percentile filter (70 percentile).

correspond to the silicide plane almost perpendicular to the α(001), the deviation is about 2.5°. The triangular nanoplates with one possible facet of α(11n) may be considered as nanocrystals having this slightly inclined facet (Fig. 3e, Fig. 4).

Another feature easily noticeable with the help of analysis of NCS maps is that coordinates of high NCS density spots calculated with respect to numbers of atoms in silicon and α-FeSi$_2$ do not coincide (Fig. S11-S13). This corresponds to the situation in the calculation with the approach used when silicon planes given at φ and Θ angles contain only a few atoms, which easily find coincidence sites in α- $FeSi_2$ highly packed planes, and vice versa. In general, a higher NCS density observed for silicon is due to its lower atom density of 0.0499 atoms/Å^3 in comparison with α-$FeSi_2$ with 0.0812 atoms/Å^3. Moreover, different areas used for the calculation may change the distribution of the maximum for the NCS densities (Fig. S11, S14) while qualitatively it does not change results. The main NCS rays remain the same. i.e. the α(11n) one. Thus, more detailed consideration of the NCS density on large interface areas is required, differentiating the sort of atom at the interface and taking into account non-equivalence of atom packing in planes parallel to interface plane between two phases. Such an approach would eliminate ambiguity in the analysis of possible interfaces. However, the required time to complete the computation would be many weeks in the case of calculation of the NCS map for one OR with a step as low as 0.5 for φ, Θ.

Therefore, when the NCS density is relatively high and similar for both cases of calculation one can expect such habit planes have a tendency to form a flat interface, i.e. one can consider mean value calculated with an NCS value obtained with respect to silicon and the α-$FeSi_2$ total amount of atoms at the interface. One can see that among possible side interfaces with α(01n) or α(11n) planes depicted on the mean NCS distribution lines on Fig. S11c, d, Fig. S12c, d the NCS higher values correspond to α(11n) planes. Furthermore, in the case of α(001)[010]//Si(001)[010] basic OR the planes lying within range of Θ ~ 30° to 85°, α(113), α(112), α(447), α(221) or plane with high Miller indices α(1 1 0.85), show the highest NCS density values Fig. S11d.

It is possible to conclude that the position of main and high NCS density peaks on the NCS distribution line may differ from those peaks observable on experimental TEM images due to uncertainty in sample position. Thus, it is more useful to consider a smoothed NCS distribution line. Here we implemented the percentile filter with parameters: 70 percentile, 80 points of the window. Mean value of the four NCS distribution lines (Fig. S11c, d, Fig. S12c, d) is represented in the article in Fig. 5. As the distribution of observable angles on experimental TEM images between α(001) and side facets of α(001)//Si(001) rectangular and triangular nanoplates (Fig. 5a) the mean smoothed NCS distribution line shows a maximum around 55 degrees, which is mainly due to α(112) and α(447) planes for α(001)[010]//Si(001)[010] basic OR. The NCS distribution line for α(001)[010]//Si(001)[110] shows an increment of the NCS density value around the α(112) position and adds an impact to the main peak on the NSC line presented on Fig. 5b.

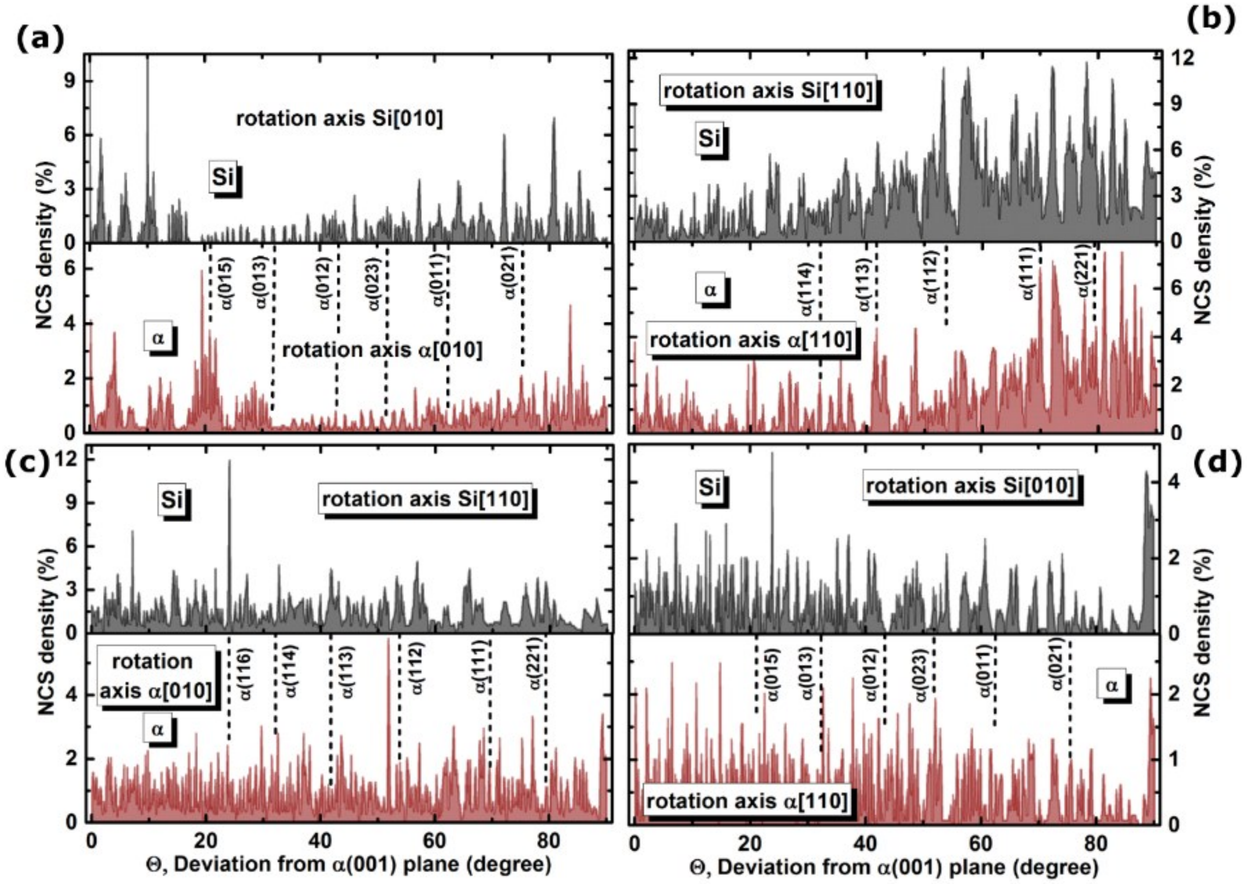

Fig. S13 α(001)[010]//Si(001)[010] orientation relationship: (a) NCS distribution line calculated at rotation around α,Si[010] direction starting from α,Si(001) plane (400x400 Å), (b) – around α,Si[110] direction; α(001)[010]//Si(001)[110] orientation relationship: (c) NCS density distribution line calculated at rotation around α[010], Si[110] direction starting from α,Si(001) plane, (d) – around α[010],Si[110] direction.

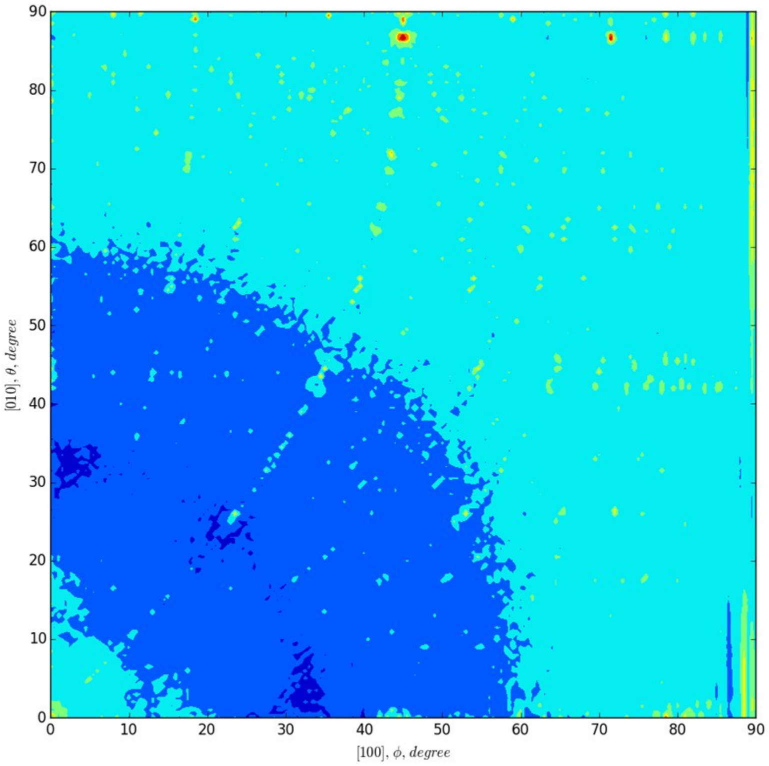

Fig. S14 Near coincidence site density maps for α(001)[100]//Si(100)[001] orientation relationship. The NCS density is the ratio between a quantity of NCS in a habit plane and the number of atoms in α-$FeSi_2$. The calculation was made on 240 x 240 Å with a step of 0.1 for φ and Θ angles.

Table S3 The data showing the angle between possible side interface for α(001)[010]||Si(001)[010] and α(001)[010]||Si(001)[110] ORs

α-FeSi$_2$ side facets	**α(001)[010]||Si(001)[010]**		**α(001)[010]||Si(001)[110]**	
	Angle between planes, °	**Si matrix planes**	**Angle between planes, °**	**Si matrix planes**
I				
α{011}	1.063	Si{021}	2.388	Si{1.5 1.5 1}
α{012}	1.31	Si{011}	0.376	Si{1 1 1.5}
α{013}	1.199	Si{0 1 1.5}	2.773	Si{112}
α{014}	1.034	Si{0 1 2}	0.292	Si{113}
α{015}	0.889	Si{0 1 2.5}	1.089	Si{113.5}
α{016}	0.772	Si{0 1 3}	1.808	Si{113.5}
II				
α{111}	0.838	Si{221}	1.492	Si{2.5 0 1}
α{112}	1.244	Si{111}	2.819	Si{1.5 0 1}
α{113}	1.36	Si{1 1 1.5}	2.992	Si{1 0 1}
α{114}	1.226	Si{112}	0.349	Si{1 0 1.5}
α{115}	1.11	Si{112.5}	1.822	Si{1 0 2}
α{116}	0.996	Si{113}	2.322	Si{1 0 2}

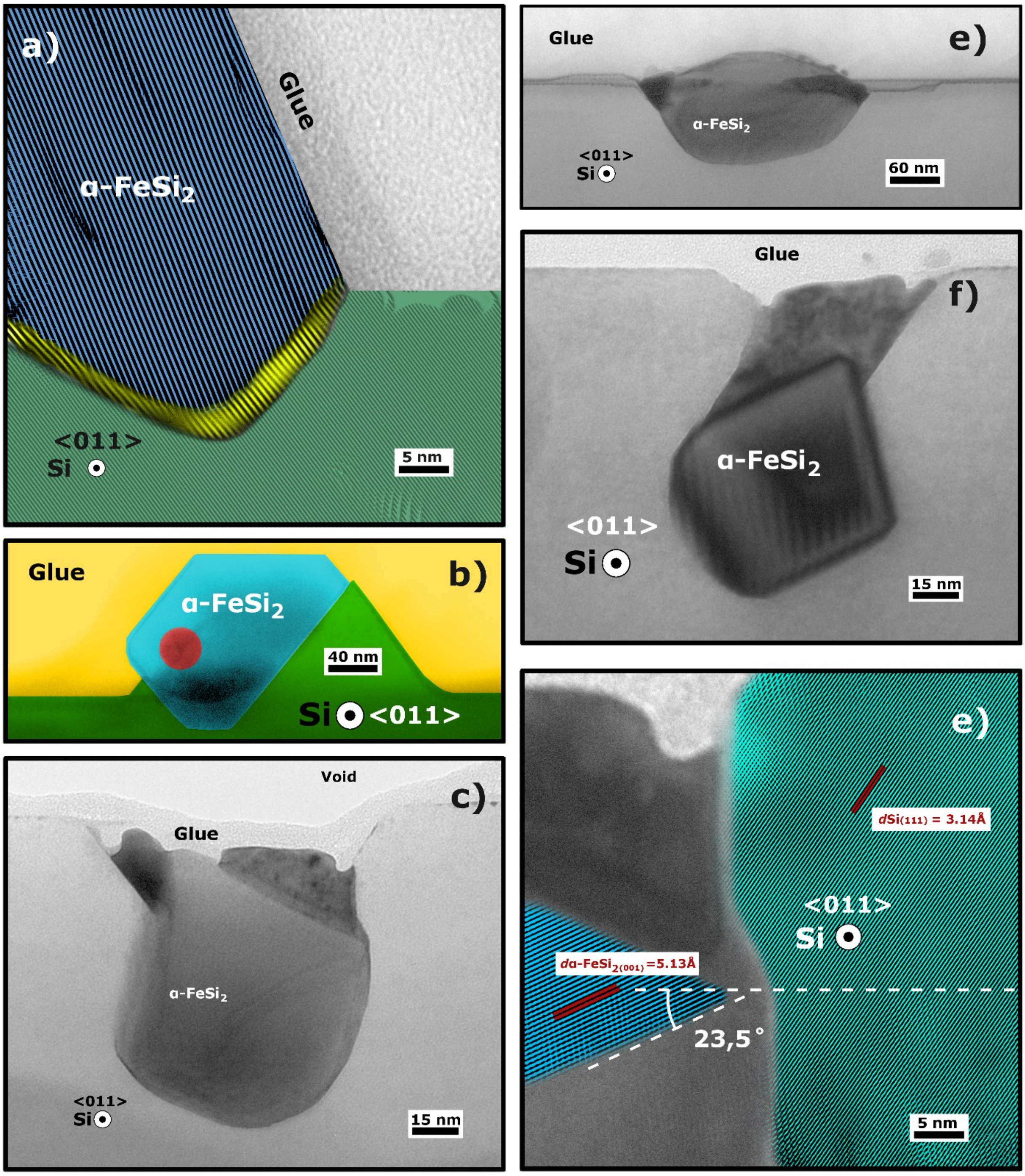

Fig. S15 TEM images of various α-FeSi$_2$ nanocrystals in the AS1 and AS2 samples.

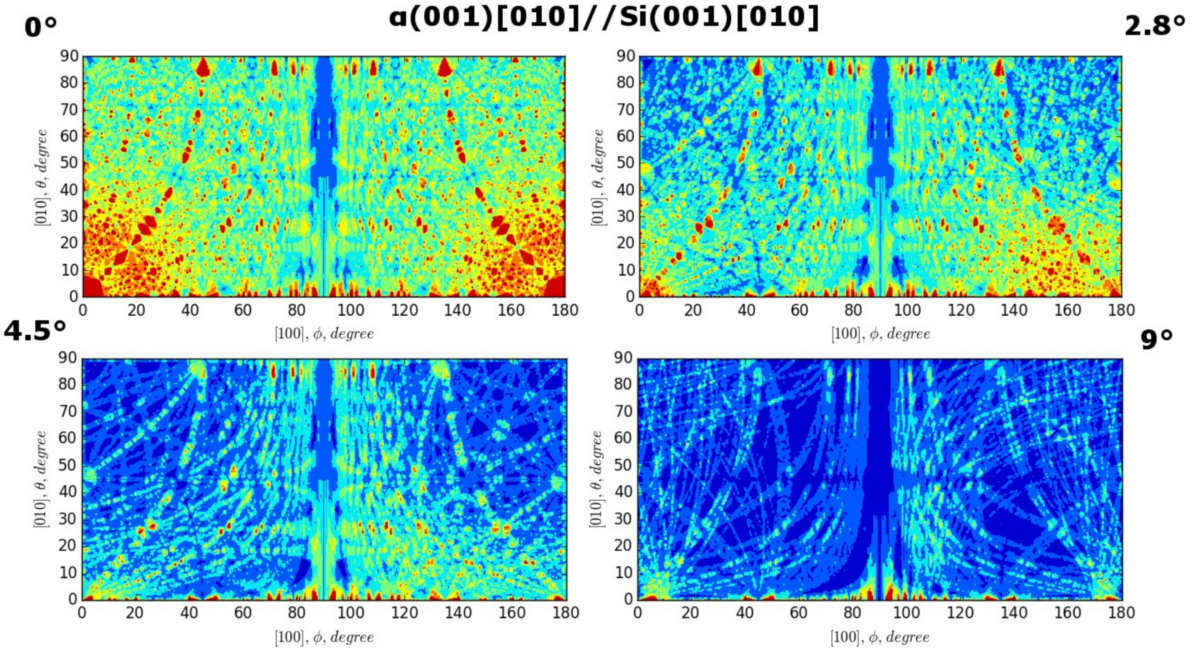

Fig. S16 Near coincidence site density maps for α(001)[100]//Si(100)[001] orientation relationship with different deviations around α[010] direction from the parallelism given by OR (φ = 0º, 2.8º, 4.5º, 9º); Calculation was made on 40 x 40 Å with a step of 0.5 for φ and Θ angles.

It is useful to note that an inclination of the main interface on the α(001)//Si(001) rectangular or triangular nanoplates (Fig. S2) does not contradict to the NCS concept. The angle between α(001) planes and Si(001) can vary in range from 2.8 to 9° (Fig. S2). Calculation of the NCS density for such deviated α(001)/2.8°-9°/Si(001) ORs (Fig. S16) reveals that the deviated α(001)|2.8°-9°|Si(001) interfaces show a high NCS density value. At lower inclination angles the α(001)||Si(001) habit plane still shows a high NCS density (φ, θ ~ 0º in Fig. S16). However, at highest deviation angle of 9° most favourable planes observed lies in the range between α(001) and α(010) planes. One can see the α(001)||Si(001) interface on the nanocrystal with the inclination of 9 degrees is shrunk in the area comparatively to the wide side interface (Fig. S2).

Table S4 Experimental lattice parameters and interplanar spacings of the α-FeSi$_2$ nanocrystals in comparison with the literature data[3,4]. The misfits are defined as $\delta = (|\mathbf{a}_1| - |\mathbf{b}_1|)/|\mathbf{b}_1|*100$ %, $\mathbf{a}_1$ is the interplanar spacing or vector length experimentally determined, $\mathbf{b}_1$ refers to the reference one.

Plane (hkl)	**d_{hkl}, interplanar spacing, Å**					**δ, interplanar spacing misfits, %**			
	Ref. [3,4]	**AS1**	**AS2**	**S1**	**S2**	**δ_{AS1}**	**δ_{AS2}**	**δ_{S1}**	**δ_{S2}**
Nanoplates, pyramid-like nanocrystals									
(001)	5.1280 5.1444	5.1044	5.1017	5.1013	5.1086	-0.46 -0.78	-0.51 -0.83	-0.52 -0.84	-0.38 -0.70
(002)	2.5640 2.5722	2.5573	2.5565	-	-	-0.26 -0.58	-0.29 -0.61	-	-
(003)	1.7093 1.7148	1.7059	1.7052	1.7047	-	-0.20 -0.52	-0.24 -0.56	-0.27 -0.59	-
(004)	1.2820 1.2861	1.2791	1.2797	-	-	-0.23 -0.54	-0.18 -0.50	-	-
{114}	1.1568 1.1607	1.0637(1)	-	-	-	-8.05 -8.36	-	-	-
Lattice parameters calculated based on interplanar distances									
a, b	2.6840 2.6955	2.71(1)	-	-	-	0.97 0.54	-	-	-
c	5.1280 5.1444	5.111(6)	-	-	-	-0.33 -0.65	-	-	-
Tetrahedrons and others with the α(111)//Si(001) OR									
(111)	1.7799 1.7873	1.7807	1.7795	1.7780	1.7817(1)	0.04 -0.37	-0.02 -0.44	-0.11 -0.52	0.10 -0.31
{110}	1.8979 1.9060	1.8951	-	1.9040	1.9067	-0.15 -0.57	-	0.32 -0.10	0.46 0.04
Lattice parameters calculated based on interplanar distances									
a, b	2.6840 2.6955	2.6801(3)	-	2.692(2)	2.6965(5)	-0.15 -0.57	-	0.32 -0.10	0.47 0.04
c	5.1280 5.1444	5.20(2)	-	4.97(2)	5.00(1)	1.4 1.08	-	-3.08 -3.39	-2.50 -2.81
Polyhedral nanobars									
(102)	1.8540 1.8609	1.8525	1.8528	1.8494	-	-0.08 -0.45	-0.06 -0.43	-0.25 -0.62	-
Trapezoid nanoplates									
{102}	1.8540 1.8609	1.8454	-	1.8569	1.8451	-0.46 -0.83	-	0.16 -0.21	-0.48 -0.85
The others									
(110)	1.8979 1.9060	1.9009	1.8985	-	-	0.16 -0.27	0.03 -0.39	-	-

Table S5 Experimentally observed and estimated α-$FeSi_2$//Si ORs. The habit planes (*hkl*) and directions [*uvw*] determining the orientation relationships are given. Other ORs which may be observed in the α-$FeSi_2$//Si nanocrystals may be found in the ESI #2. The misfits are defined as $\delta_1 = (|\mathbf{a_1}| - |\mathbf{b_1}|)/|\mathbf{b_1}|*100$ %, $\delta_2 = (|\mathbf{a_2} - \mathbf{b_2}|/|\mathbf{b_2}|)*100$ %, $\mathbf{a_1}$ is the close-packed vector length in the surface unit cell of α-$FeSi_2$ crystal, $\mathbf{b_1}$ refers to the silicon one, $\mathbf{a_2}$ and $\mathbf{b_2}$ refer to the second pair of any vector in the α-$FeSi_2$ and silicon unit cell, respectively.

(hkl)	**(hkl)**	**[uvw]**	**[uvw]**	**δ_1, misfit, %**	**[uvw]**	**[uvw]**	**δ_2, misfit, %**	**$\tilde{\varepsilon}$, strain, %**
rectangular nanoplates								
α(001)	Si(001)	α[020]	Si[010]	1.15	α[200]	Si[100]	-1.15	1.01
α(001)	Si(001)	α[030]	Si[1-10]	4.84	α[300]	Si[110]	4.84	4
α(1-1-2)	Si(1-1-1)	α[220]	Si[110]	-1.15	α[201]	Si[101]	3.58	2.47
α(1-1-2)	Si(0-23)	α[330]	Si[200]	4.84	α[3-33]	Si[032]	2.258	2.00
α(0-11)	Si(0-12)	α[200]	Si[100]	-1.15	α[022]	Si[021]	4.67	2
α(0-11)	Si(3-12)	α[300]	Si[110]	4.84	α[033]	Si[1-13]	3.60	2.12
tetrahedrons								
α(1-1-1)	Si(001)	α[220]	Si[110]	-1.15	α[202]	Si[2-10]	4.84	3.01
α(113)	Si(-225)	α[-220]	Si[110]	-1.15	α[-6-64]	Si[-55-4]	4.84	6.43
α(22-3)	Si(-55-6)	α[-220]	Si[110]	-1.15	α[12 12 16]	Si[10-10 -17]	4.84	2.36
α(221)	Si(1-19)	α[-220]	Si[110]	-1.15	α[-1-14]	Si[-992]	4.84	1.04
polyhedral nanobars								
α(-102)	Si(001)	α[201]	Si[110]	-3.34	α[030]	Si[1-10]	4.84	2.08
trapezoid nanoplates (buffer layer)								
α(010)	Si(2-2-3)	α[300]	Si[110]	4.84	α[006]	Si[3-34]	2.84	2.02
α(0-14)	Si(3-3-5)	α[300]	Si[110]	4.84	α[10 8 2]	Si[613]	3.76	2.99

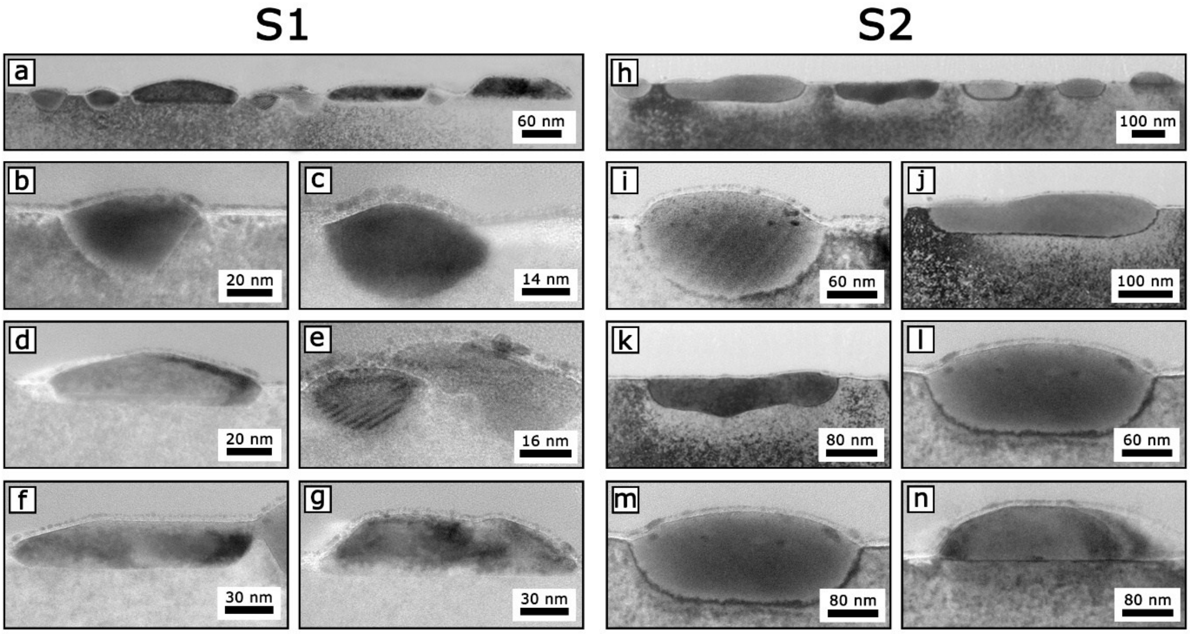

Fig. S17 TEM images of various α-$FeSi_2$ nanocrystals for the S1 and S2 samples.

References

1 I. A. Tarasov, I. A. Yakovlev, M. S. Molokeev, M. . Rautskii, I. V. Nemtsev, S. N. Varnakov and S. G. Ovchinnikov, *Mater. Lett.*, 2016, **168**, 90–94.

2 I. A. Tarasov, M. A. Visotin, A. S. Aleksandrovsky, N. N. Kosyrev, I. A. Yakovlev, M. S. Molokeev, A. V. Lukyanenko, A. S. Krylov, A. S. Fedorov, S. N. Varnakov and S. G. Ovchinnikov, *J. Magn. Magn. Mater.*, 2017, **440**, 144–152.

3 B. Aronsson, D. H. Templeton, S. Rundqvist, E. Varde and G. Westin, *Acta Chem. Scand.*, 1960, **14**, 1414–1418.

4 W. Miiller, J. M. Tomczak, J. W. Simonson, G. Smith, G. Kotliar and M. C. Aronson, *J. Phys. Condens. Matter*, 2015, **27**, 175601.